Title

Regional Aβ-tau interactions promote onset and acceleration of Alzheimer's disease tau spreading

Journal

Neuron, 110(12)

ISSN

0896-6273

Authors

Lee, Wha Jin

Brown, Jesse A

Kim, Hye Ryun

et al.

Publication Date

2022-06-01

DOI

10.1016/j.neuron.2022.03.034

Peer reviewed

HHS Public Access

Author manuscript

Neuron. Author manuscript; available in PMC 2023 June 15.

Published in final edited form as:

Neuron. 2022 June 15; 110(12): 1932–1943.e5. doi:10.1016/j.neuron.2022.03.034.

Regional Aβ-tau interactions promote onset and acceleration of Alzheimer's disease tau spreading

Wha Jin Lee[1],

Jesse A. Brown[2,3],

Hye Ryun Kim[1,4],

Renaud La Joie[2,3],

Hanna Cho[5],

Chul Hyoung Lyoo[5],

Gil D. Rabinovici[2,3,6],

Joon-Kyung Seong[1,7,*,†],

William W. Seeley[2,3,8,9,*,†]

Alzheimer's Disease Neuroimaging Initiative‡

[1]Korea University, School of Biomedical Engineering, Seoul, 02841, Korea

[2]University of California, San Francisco, Memory and Aging Center, Department of Neurology, San Francisco, CA 94143, USA

[3]University of California, San Francisco, Weill Institute for Neurosciences, San Francisco, CA 94143, USA

[4]Korea University, Global Health Technology Research Center, College of Health Science, Seoul, 02841, Korea

[5]Gangnam Severance Hospital, Department of Neurology, Seoul, 06273, Korea

[*]Correspondence to: bill.seeley@ucsf.edu (W.W.S.); jkseong@korea.ac.kr (J.S.).

[†]These authors contributed equally.

Author contributions

W.L., J.S. and W.W.S. conceived and designed the study. W.L., H.K., H.C. and C.L. contributed to data acquisition and processing. W.L. performed the experimental work and W.L., J.A.B., J.S. and W.W.S. analyzed and interpreted the results. W.L., J.A.B., J.S. and W.W.S. wrote the manuscript, and J.S. and W.W.S. substantively revised it. All authors participated in the discussion and critically reviewed the paper.

[‡]Data used in preparation of this article were obtained from the Alzheimer's Disease Neuroimaging Initiative (ADNI) database (adni.loni.usc.edu). As such, the investigators within the ADNI contributed to the design and implementation of ADNI and/or provided data but did not participate in analysis or writing of this report. A complete listing of ADNI investigators can be found at: http://adni.loni.usc.edu/wp-content/uploads/how_to_apply/ADNI_Acknowledgement_List.pdf

Declaration of interests

W.W.S. received compensation as a lecturer for Corcept Therapeutics and as a consultant for Guidepoint Global Consulting and GLG Council. G.D.R. receives research support from the National Institutes of Health, Alzheimer's Association, American College of Radiology, Rainwater Charitable Foundation, Gift from Edward and Pearl Fein, Avid Radiopharmaceuticals, Eli Lilly, Life Molecular Imaging, GE Healthcare, Genentech. He has served as a consultant for Axon Neurosciences, Eisai, GE Healthcare, Merck, Genentech, and Roche. He serves on a data safety monitoring board for Johnson & Johnson. He is an Associate Editor for JAMA Neurology. A subset of the authors has filed provisional patent no. 63/085,749 in the U.S. based on this work.

[6]University of California, San Francisco, Department of Radiology and Biomedical Imaging, San Francisco, CA 94143, USA

[7]Korea University, Department of Artificial Intelligence, Seoul, 02841, Korea

[8]University of California, San Francisco, Department of Pathology, San Francisco, CA 94143, USA

[9]Lead Contact

Summary

Amyloid-beta and tau are key molecules in the pathogenesis of Alzheimer's disease, but how these proteins interact to promote disease remains unclear. Here, by combining cross-sectional and longitudinal molecular imaging and network connectivity analyses in living humans, we identified two amyloid-beta/tau interactions associated with the onset and propagation of tau spreading. First, we show that the lateral entorhinal cortex, an early site of tau neurofibrillary tangle formation, is subject to remote, connectionally mediated amyloid-beta/tau interactions linked to initial tau spreading. Second, we identify the inferior temporal gyrus as the region featuring the greatest local amyloid-beta/tau interactions and a connectivity profile well-suited to accelerate tau propagation. Taken together, our data address long-standing questions regarding the topographical dissimilarity between early amyloid-beta and tau deposition.

eTOC Blurb

"Lee et al. show that the natural history of AD traverses a critical period that begins once Aβ emerges within entorhinal cortex (EC)-connected regions, continues as tau spreads from the EC into connected mesial temporal and limbic regions, and may end once Aβ and tau interact within the inferior temporal gyrus propagation hubs, whose connections are well-suited to facilitate widespread neocortical tau propagation."

Keywords

Alzheimer's disease; tau; amyloid-beta; PET; connectome; DTI

Introduction

Brain parenchymal amyloid-beta (Aβ) deposition and tau neurofibrillary tangle formation are the defining pathological features of Alzheimer's disease (AD) (Braak et al., 2006, Jagust, 2018, Musiek and Holtzman, 2012). Aβ has been proposed to trigger tau spreading (Musiek and Holtzman, 2012, Jagust, 2018), but the spatial incongruity of Aβ and tau during early AD has cast doubt on this hypothesis (Jagust, 2018). Whereas Aβ deposition begins in heteromodal association neocortices (Thai et al., 2002), the earliest forebrain neurofibrillary tangles are seen within the lateral entorhinal cortex (Hyman et al., 1984). From there, tau spreads into other mesial temporal memory structures but rarely beyond the basal temporal cortex in the absence of widespread neocortical Aβ deposition (Crary et al., 2014, Johnson et al., 2016, Sanchez et al., 2021a). Considering these observations, how can remote neocortical Aβ influence early pathological tau, triggering it to leave the

entorhinal cortex? How, in turn, does Aβ facilitate widespread tau propagation throughout the neocortex?

Recent *in vivo* evidence supports the view that tau pathophysiology exhibits a non-linear acceleration during the natural history of AD (McDade et al., 2018, Jack et al., 2010), and understanding the basis for this acceleration represents an important priority for AD research. Human post-mortem (Braak and Del Tredici, 2011, Kim et al., 2019), *in vivo* brain imaging (Zhou et al., 2012, Raj et al., 2015, Brown et al., 2019, Vogel et al., 2020, Ossenkoppele et al., 2019, Franzmeier et al., 2020), and model-based (Liu et al., 2012, Clavaguera et al., 2013) studies have converged to suggest that transneuronal tau spreading likely contributes to the progressive large-scale network degeneration seen in AD and other tau-based disorders. We and others have used the normative functional and structural connectome to predict the spatial patterning and spread of atrophy (Zhou et al., 2012, Raj et al., 2015, Raj et al., 2012), and early tau-PET studies suggest connectivity-related tau patterning in AD (Ossenkoppele et al., 2019, Vogel et al., 2020, Sepulcre et al., 2018). To date, however, no study has provided a connectivity-based molecular anatomical framework for understanding the onset and acceleration of tau spreading in AD.

In this study, we combined *in vivo* molecular imaging and large-scale brain network mapping techniques to address the long-standing questions of how regional Aβ and tau interact to promote the onset and acceleration of tau spreading in individuals with presymptomatic and prodromal AD. Our findings suggest that (1) remote Aβ incites tau spreading by interacting, via long-range connections, with tau in the entorhinal cortex whereas (2) local Aβ-tau interactions in the inferior temporal gyrus (ITG) facilitate widespread, connectivity-based tau propagation into neocortical regions that become tau-positive during the tau acceleration phase.

Results

Early entorhinal tauopathy and exponential tau acceleration during prodromal AD

To capture the non-linear acceleration of AD tau spreading (Figure 1A), we studied individuals enrolled in a multicenter observational study, the AD Neuroimaging Initiative (ADNI), who underwent cross-sectional ^{18}F-florbetapir-PET (henceforth “amyloid-PET”) and ^{18}F-flortaucipir-PET (henceforth “tau-PET”) imaging (see Table 1). First, we mapped regions of tau-PET positivity in presymptomatic (Aβ+, cognitively normal, CN, n = 67) and prodromal AD (Aβ+, early (n = 28) and late (n = 17) mild cognitive impairment, MCI, see Methods). Tau-PET positivity in presymptomatic AD was mild, but the entorhinal cortex (EC; [A28/34, A35/36r]) stood out as a region with high mean tau-PET signal (Figure 1B). This tau-PET mapping approach also revealed the expected sharp increase in brain-wide tau deposition in patients with late MCI. Second, we calculated the number of tau-positive brain regions for each subject within these groups (see Methods). Based on the resulting frequency distribution for regional tau burden, we constructed a pseudo-longitudinal disease severity order, with the least severe subjects being those with the fewest tau-PET-positive regions. This approach identified the EC (A28/34, A35/36r) as the earliest region to become tau-positive, based on the frequency distribution within each hemisphere. Overall, these approaches, which use cross-sectional data to make longitudinal inferences, converged to

broadly reproduce the canonical stages of tau neurofibrillary tangle formation inferred from human neuropathological studies (Braak and Braak, 1991) (see Table S1). Most importantly, this dataset enabled us to identify an apparent "acceleration phase" of exponential spreading in the spatial extent of tau-PET positivity and, in turn, the regions that exhibit tau-PET positivity before, during, and after this tau acceleration phase (Figure 1C). The tau regional spreading order was generally robust across a range of tau *W*-score thresholds (Figure S1), and the key findings shown in Figure 1 were replicated in an independent sample of older subjects from across the AD clinical spectrum (henceforth, "Korean validation dataset", see Methods and Figures S1 and S2). Importantly, the Korean validation dataset included a larger proportion of subjects with more advanced clinical AD (see Table 1), suggesting that the identified acceleration phase did not result simply from analyzing an ADNI sample skewed toward early AD stages.

A network flow-based model identifies the inferior temporal gyri as key tau propagation hubs

To clarify the anatomical basis for accelerated tau spreading, we used diffusion tensor imaging to construct a normative "connectome", a matrix describing the group-level structural connectivity between each pair of brain regions. We then used this connectome to create a network flow-based model for simulating tau propagation along region-to-region macro-scale connections (Figure 2A). This model enabled us to identify brain regions well-positioned to promote widespread tau aggregation (henceforth, "propagation hubs") and to clarify how Aβ deposition relates to initial and accelerated tau spreading. Applying the principles of graph theory, we modeled connectivity-mediated tau spreading based on maximum inter-nodal flow, which considers multiple distinct paths between any two nodes (Figure 2A). We then searched a pool of 213 regions, after removing regions prone to off-target tau-PET binding (i.e., radiotracer binding to non-tau targets, see Table S2), with the goal of identifying tau propagation hubs. Specifically, we searched a library of normative network flow-based connectivity maps, each based on a single candidate brain region or "seed", (Figure 2B), seeking to identify regions whose connectivity most resembles the regions into which tau spreads during the tau acceleration phase. To this end, we estimated the goodness-of-fit (GOF) between each seed's map and the topography of the tau acceleration phase, representing the tau acceleration phase by generating seven pairs of binary inner and outer masks across a range of spatial extents. Masks were gradually expanded to mimic tau propagation (Figure S3) and to avoid potential influences of arbitrary thresholding and mask definition. Finally, we identified propagation hubs, using a stringent set of criteria, as those nodes with significant GOF scores (permutation-based one-sample t-test, Bonferroni corrected $p < 0.05$) across all seven inner/outer mask pairs (see Methods). Based on this brain-wide search strategy, the left and right inferior temporal gyri (ITG) emerged, independently, as propagation hubs (Figure 2C), and this finding was stable after varying the total number of inner/outer mask pairs used to represent the acceleration phase (Table S3).

As expected, the network flow-based connectivity maps seeded by these ITG propagation hubs were strongly correlated with the topography of tau deposition seen in subjects representing the acceleration phase (contrasted with pre-acceleration phase subjects; Figure

3A and 3B; see Methods), and those correlations were stronger than seen for other brain regions (based on null hypothesis distributions, Figure 3C) (Scott et al., 2020). Compared to other network-based propagation models developed through our previous work (Brown et al., 2019, Zhou et al., 2012), the network flow-based model produced the highest correlations between the ITG propagation hub connectivity pattern and the acceleration phase tau deposition topography (see Figure S4), justifying our use of the network flow-based model for propagation hub identification. Applying the same propagation hub identification procedure to the Korean validation dataset, we again identified the two ADNI-derived ITG areas, and the connectivity of these regions correlated strongly with the pattern of acceleration phase tau deposition topography (Figure S4B). We also identified three additional putative propagation hubs, all within the ITG regions bilaterally (see Figure S5). Because tau-PET image analysis methods continue to evolve, we also reproduced these key findings after varying several methodological steps that remain unsettled in the field (see Tables S4 and S5).

Remote and local Aβ-tau interactions are associated with initial and accelerated tau spreading

AD has been conceptualized as an Aβ-triggered tauopathy (Musiek and Holtzman, 2012), but to date it has been difficult to reconcile this concept with the topographical discordance between early Aβ and tau deposition in humans. Having (1) confirmed the EC as the forebrain region from which initial tau spreading occurs and (2) identified the bilateral ITG regions as tau propagation hubs, we sought to determine whether and how Aβ might interact with tau in the EC and ITG to induce and accelerate tau spreading. To this end, we developed a network-based model to estimate two types of Aβ-tau interaction: remote and local (Figure 4A). Remote interactions were conceived as arising from each tau-positive region's connectivity to Aβ-positive regions. More specifically, we imagined that tau-positive regions contain tau-positive neurons, whose axons travel to and form synapses with neurons residing in Aβ-positive regions. Specific Aβ species may, in turn, prove toxic to those synapses or may otherwise influence axons arriving from or departing to remotely connected, tau-positive neurons, thereby triggering a long-range interaction with the tau-positive region. Local interaction, in contrast, was conceived as the direct comingling of parenchymal Aβ and aggregating tau within a given brain region (He et al., 2018).

Calculation of remote Aβ-tau interactions required three steps. First, we calculated each region-of-interest's weighted connectivity strength, derived from the healthy structural connectome, to all other regions. Second, we multiplied each connectivity strength by the magnitude of Aβ-deposition within the connected region and summed these products to calculate a connectivity-weighted remote Aβ influence metric. Finally, the remote Aβ influence metric was multiplied by the magnitude of tau deposition within the region-of-interest (Figure 4A). To rank regions according to their remote Aβ-tau interactions, we again applied the frequency distribution method, assuming that regions with the earliest remote Aβ-tau interactions would be those in which these connectivity-mediated interactions were detected in the largest proportion of patients (see Methods). Using this approach, we found that the lateral entorhinal cortex (EC; [A35/36r]) ranked first among 213 brain regions (Figures 4B and S7). Based on absolute levels, the lateral EC showed significantly

greater remote Aβ-tau interaction than the median of all other brain regions (*t*: 3.63/2.61, FDR-corrected *p*-value: 0.001/0.017, left/right EC). This finding was stable across a range of tau *W*-score thresholds (Figure S6) and alternative tau-PET analysis methods (Tables S4 and S5) and was broadly replicated in the Korean validation dataset, in which the lateral EC had the highest median remote Aβ-tau interaction rank of any brain region (EC left: 4th, EC right: 1st; Figures S6 and S7). Robustness of this finding across a range of *W*-score thresholds was even more evident in the Korean validation dataset, perhaps because this dataset represents a more homogeneous cohort evaluated at a single center.

To calculate local Aβ-tau interactions, we multiplied each region's local Aβ deposition (amyloid-PET SUVR value) by its tau-PET *W*-score. Although the procedures for calculating local Aβ-tau interactions and those for identifying propagation hubs were completely independent, the left and right ITG propagation hubs emerged as the highest-ranking regions, brain-wide, for local Aβ-tau interaction (Figures 4B and S7). Local Aβ-tau interaction scores for the left and right ITG were significantly greater than the median of all other regions (*t*: 3.77/4.28, FDR-corrected *p*-value: <0.001/<0.001, left/right ITG). This finding was stable across a range of tau *W*-score thresholds (Figure S6) and alternative tau-PET analysis methods (Tables S4 and S5). These findings were also broadly reproduced in the Korean validation dataset (Figures S6 and S7), in which the ITG hubs for each hemisphere ranked in the top 4 for local Aβ-tau interaction within that hemisphere (ITG7, right: 4th; ITG4, left: 3rd), with the few higher-ranking regions being adjacent basal temporal areas.

Longitudinal tau aggregation trajectories support the Aβ-tau interaction model

In the preceding analyses, we used cross-sectional data to make longitudinal inferences about the natural history of AD. This strategy enabled us to derive a tau regional spreading order based on a sufficient sample size; nonetheless, the pseudo-longitudinal approach cannot directly test the within-subjects temporal predictions made by our model. To address this limitation, we collected all subjects in the ADNI (n = 135) and Korean (n = 169) cohorts who had undergone at least one follow-up structural MRI and tau-PET scan (See Table 1). Because the two longitudinal samples were relatively small, we combined them into a single ADNI/Korean longitudinal MCI cohort after regularizing the two datasets separately using the *W*-score approach (see Methods). Using this combined cohort, we first determined the regional tau accumulation rate, defined as the annualized change in the tau-PET *W*-score. As expected, tau accumulation in subjects with Aβ+ MCI (n = 68) is most prominent in basal temporal areas and, to a lesser extent, fronto-parietal heteromodal association cortices (Figure 5A). Next, we returned to our library of normative network flow-based maps, one derived from each brain region, to determine the spatial correlation between each region's connectivity pattern and the longitudinal tau accumulation seen in Aβ+ MCI Remarkably, mirroring the cross-sectional findings, the ITG regions again stood out as the regions whose connectivity best matched the longitudinal tau accumulation pattern (Figure 5A).

Next, to test the longitudinal predictions arising from the Aβ-tau interaction components of our model, we established quantitative thresholds for Aβ- and tau-PET positivity within each region brain-wide (see Methods). We then used these thresholds to group subjects,

irrespective of their clinical label, based on their baseline Aβ and tau status in the bilateral EC and ITG regions-of-interest previously identified through the cross-sectional remote and local Aβ-tau interaction analyses. We quantified tau spreading into downstream regions by averaging the annualized tau accumulation rates within the 30 regions downstream of the regions-of-interest, based on the established tau spreading order (Figure 1C and Table S1). For the EC, we predicted that downstream tau spreading would be greatest when the EC is tau-positive at baseline, with little influence by the local co-presence of Aβ. Critically, however, our model predicts that regions downstream to the EC will show greater tau accumulation insofar as the EC is subjected to remote Aβ-tau interaction. Each of these EC-based predictions was supported by our longitudinal data (Figure 5B; *t*: 0.32/−0.98, *p*-value: 0.749/0.330, left/right EC, for influence of local Aβ; Mann-Whitney U test *Z*: 1.73/2.73, one-tailed *p*-value: 0.041/0.003, left/right EC; for influence of remote Aβ, Figure 5B inset). Regarding the ITG propagation hubs, our model predicts accelerated tau spreading when Aβ and tau interact locally within the ITG. Here, we found that regions downstream to the ITG accumulated more tau in subjects who transitioned from having only Aβ in the ITG to having both Aβ and tau (Figure 5C inset; Mann-Whitney U test *Z*: 4.23/4.04, *p*-value: <0.001/<0.001, left/right ITG, for the influence of emerging Aβ-tau co-positivity). Emergent Aβ-tau co-positivity in the ITG was invariably the result of an Aβ-positive ITG that became tau-positive at follow-up. The longitudinal EC and ITG findings reported here were stable across a range of downstream region numbers (Table S6).

Two pivotal Aβ-tau interactions in the natural history of AD

The findings outlined above suggest two major inflection points in the molecular-anatomical pathogenesis of AD. The first occurs when neocortical Aβ emerges within multiple neocortical and limbic regions connected to the entorhinal cortices. This remote, connectionally mediated interaction between Aβ and EC tau may induce tau to undergo biophysical changes that propel it to spread out of the entorhinal areas and into nearby, connected regions in the hippocampus, amygdala, and basal temporal cortices. The second pivotal moment occurs when tau neurofibrillary changes reach the ITG, where tau can locally interact, for the first time, with pre-existing Aβ, catalyzing widespread tau propagation into Aβ-positive and ITG-connected neocortical regions whose degeneration ultimately gives rise to dementia (Sepulcre et al., 2018). If these Aβ-tau interactions occur in sequence, as we hypothesize, then metrics capturing these two phenomena should obey a nonlinear relationship in which the EC remote Aβ-tau interaction rises first, before giving way to a rise in local Aβ-tau interaction within the ITG (Figure 6A; see Methods). Plotting these metrics across our discovery and validation cohorts, using cross-sectional and longitudinal data, strongly supported this prediction, demonstrating a fundamental arc of disease progression across and within individuals (Figure 6B). Quadratic regression models based on the mean (left/right) cross-sectional values fit both datasets well (ADNI: R^2 = 0.664, Korean: R^2 = 0.652), significantly better than did linear functions (ADNI: R^2 = 0.658 / F (testing for the difference between quadratic and linear fit) = 7.022, p = 0.008; Korean: R^2 = 0.541 / F = 108.02, p = 2e-16) (Indrayan and Malhotra, 2017). Focusing these analyses on subjects with at least one APOE ε4 allele further emphasized the nonlinear relationship (ADNI: R^2 = 0.748 / F (testing for the difference between quadratic and linear fit) = 8.042, p = 0.005; Korean: R^2 = 0.630 / F = 26.83, p = 1e-6), perhaps because APOE ε4

carriers more often develop a typical anatomical progression that begins in medial temporal lobe memory structures (Wolk et al., 2010).

Based on the two pivotal Aβ-tau interactions, we stratified subjects into one of four groups: (1) “tau-negative” in EC, (2) insufficient EC remote Aβ-tau interaction to promote tau spreading (“latent tau”), (3) sufficient EC remote Aβ-tau interaction but minimal ITG local Aβ-tau interaction (“spreading tau”), and (4) sufficient ITG local Aβ-tau interaction (“propagating tau”). Figure 6C shows subject stratification assignments overlaid on the pseudo-longitudinal subject order derived from the tau frequency distribution approach. Using this stratification method, subjects assigned to the “spreading tau” group fall just before or shortly after the start of the tau acceleration phase, whereas those designated “propagating tau” are nearly all found within and beyond the acceleration phase. As expected, longitudinal subjects within the “spreading” and, in particular, “propagating” tau groups showed dramatically greater whole-brain annualized tau accumulation (Figure 6D). Expert recommendations for the use of the amyloid-lowering drug, aducanumab, emphasize the importance of positive AD biomarkers and a clinical label of MCI or mild dementia (Cummings and Salloway, 2021). Therefore, it is important to note that the model-driven subject stratification method presented here overlays inconsistently on the biomarker-anchored clinical groupings conventionally used in AD clinical trials (Figure 6E and Table S7). For example, subjects in the “spreading tau” group, whom we hypothesize will benefit most from amyloid-lowering therapy, represent only 14.4% of the overall Aβ+ MCI group. These findings raise the possibility that a molecular-anatomical definition of disease stage may outperform clinical labels in predicting clinical responsiveness to amyloid-lowering and other AD therapies.

Discussion

For decades, AD researchers have questioned how remote Aβ can stimulate neurofibrillary tauopathy to spread beyond the medial temporal lobe during the preclinical stages of AD (Musiek and Holtzman, 2012, Jagust, 2018). The present work shows that these early Aβ-tau interactions are likely mediated, at least in part, by long-range neural connections between the entorhinal cortex and brain regions in which early Aβ deposition occurs. More recent neuroimaging studies have emphasized a tau acceleration phase, in which frontal, temporal, and parietal heteromodal association cortex tauopathy takes hold in patients with late MCI, heralding the transition to dementia (Sanchez et al., 2021a, Sanchez et al., 2021b). Our findings identify the bilateral ITG regions as key propagation hubs whose connectional profile is poised to disseminate tau throughout the neocortex, perhaps facilitated by local Aβ-tau interactions.

Tau spreading mechanisms remain a focus of intensive study, and transneuronal spreading is but one among several proposed mechanisms. The present neuroimaging analyses, conducted at the spatial resolution of brain regions and major fiber pathways, were not designed to address all potential cellular mechanisms or to estimate their relative contributions. Rather, we worked from the assumption that transneuronal spreading makes at least some contribution to tau progression in AD even if other factors, such as shared regional vulnerability, local spreading, and other mechanisms contribute. In that regard, it is

somewhat remarkable that a model based on transneuronal spreading provides such a strong fit to the experimental data. Nonetheless, not all of our findings fit the connectivity-based model. For example, not all participants with early AD conformed to the tau spreading pseudo-order derived from cross-sectional tau-PET data (Figure 1C). This variability may reflect heterogeneous AD anatomical trajectories (Vogel et al., 2021), connectivity-independent tau spreading mechanisms, or a combination of these factors. Although our longitudinal data strongly supported the temporal predictions of our model, we observed some overlap in tau accumulation rates among patients who did or did not become newly co-positive for Aβ and tau in the ITG propagation hubs at follow-up (Figure 5C). This overlap could reflect involvement of non-ITG propagation hubs, PET tracer insensitivity to early tau deposition, or connectivity-independent tau progression. Additional research is needed to resolve these possibilities and to further refine the model proposed here.

A limitation of the current study is the use of a single structural connectome derived from healthy control subjects. DTI tractography methods can result in erroneously estimated connections (Maier-Hein et al., 2017), and early-stage AD may alter the connectome in ways that could influence our model-based predictions. As in our previous work (Zhou et al., 2012, Brown et al., 2019), we used the normative connectome to model disease spreading based on the assumption that major changes in the fundamental connectome architecture are unlikely even if individual edge weights may be influenced by disease. Furthermore, we employed a network flow-based tau spreading model; this model reflects all possible paths between source and target regions, providing robustness to minor errors in single-edge connectivity estimation. A next step in the development of this model will be to incorporate individual patient functional and/or structural connectomes to evaluate whether and how disease-related connectivity changes modulate tau spreading.

Conclusion

Our findings address a long-standing question about the pathogenesis and progression of AD by placing early Aβ-tau interactions within a connectivity-based molecular-anatomical framework. This framework suggests that the natural history of AD traverses a critical period that begins once Aβ emerges within EC-connected regions, continues as tau spreads from the EC into connected mesial temporal and limbic regions, and may end once Aβ and tau interact within the ITG propagation hubs, whose connections are well-suited to facilitate widespread neocortical tau propagation. The efficacy of Aβ-lowering drugs may depend on the timing of their delivery (Mintun et al., 2021), and the critical period defined here can now be evaluated as a potential therapeutic window. Additional work is needed to determine whether subject stratification methods based on this model can help predict responsiveness to Aβ-lowering and other AD therapeutic strategies.

STAR Methods

Resource availability

Lead contact—Further information and requests for resources should be directed to and will be fulfilled by the lead contact, William Seeley (bill.seeley@ucsf.edu).

Materials availability—This study did not generate new unique reagents.

Data and code availability—All data reported in this paper will be shared by the lead contact upon request. All original code has been deposited at GitHub and is publicly available as of the date of publication. DOIs are listed in the key resources table. Any additional information required to reanalyze the data reported in this paper is available from the lead contact upon request.

Experimental model and subject details

Participants—We included participants from two non-overlapping datasets for this study: the discovery dataset and the validation dataset. The discovery dataset consisted of participants from the Alzheimer's Disease Neuroimaging Initiative (ADNI, http://adni.loni.usc.edu/) and includes patients with AD-type dementia, mild cognitive impairment (MCI), and cognitively normal age-matched controls. All participants underwent structural magnetic resonance imaging (MRI) scans and positron emission tomography (PET) using ^{18}F-florbetapir (AV45) for Aβ and ^{18}F-flortaucipir (AV1451) scans for tau. 187 cognitively normal (CN) subjects, 64 patients with early MCI (early MCI), 30 patients with late MCI (late MCI), and 11 patients with AD dementia were used for the discovery dataset. Detailed diagnostic criteria were previously reported (http://adni.loni.usc.edu/methods/) (Petersen et al., 2010). Of the 292 subjects available, four CN subjects, one early MCI patient, and two AD-type dementia patients were excluded due to poor co-registration quality between MRI and PET scans. One early MCI patient and one CN subject were excluded due to poor pre-processing during Freesurfer-based image analysis. The ADNI sample size for the main analyses was 283 (Table 1). We also included 95 CN subjects from ADNI to construct the healthy structural connectome. These participants satisfied identical diagnostic criteria as the previous CN subjects but were chosen because they had undergone structural MRI scans and diffusion-weighted MRI (DWI) scans suitable for diffusion tractography. Of these 95 subjects, 49 were also included in the discovery dataset used for PET analysis.

The validation dataset included participants clinically diagnosed at Gangnam Severance Hospital, South Korea, from January 2015 to July 2016 (Table 1). This study was approved by the institutional review board of Gangnam Severance Hospital and written informed consent was obtained from all subjects. All participants in the validation dataset underwent structural MRI, as well as^{18}F-florbetaben PET for Aβ and ^{18}F-flortaucipir PET for tau. The participants included 96 CN subjects showing normal performance on neuropsychological tests and no abnormalities on brain MRI, as well as 84 patients with amnestic MCI (aMCI) and 71 with AD-type dementia fulfilling the National Institute on Aging-Alzheimer Association diagnostic criteria for "MCI due to AD with intermediate or high likelihood" (Albert et al., 2011) and "probable dementia with evidence of the AD pathophysiologic process" (McKhann et al., 2011), respectively. Detailed diagnostic criteria for all three clinical groups have been described (Cho et al., 2019).

For longitudinal analyses, we downloaded additional image data from the ADNI repository in January 2021. All participants had baseline scans satisfying the same criteria used for the cross-sectional analyses and had undergone follow-up structural MRI and flortaucipir PET

scans. Due to the limited samples available, we included all MCI subjects and considered early and late MCI together (Table 1). With 19 newly added subjects after excluding 4 due to image co-registration errors, 72 CN subjects, 55 patients with MCI (amyloid-PET-positive: 32), and 8 patients with AD dementia were available for the ADNI discovery dataset. In the Korean validation dataset, 169 participants including 74 CN subjects, 59 patients with amnestic MCI (amyloid-PET-positive: 36), and 36 patients with dementia (amyloid-PET-positive: 28) had follow-up scans. After calculating mean annualized change in tau-PET *W*-scores across all ROIs, four subjects with extreme outlier values, defined as any values more than 3 times the interquartile range above the third quartile, were removed from the longitudinal analyses (Hoaglin et al., 2000).

Method details

Image acquisition—For the discovery (ADNI) dataset, structural MRI and PET scans were downloaded on April 2019 from the ADNI repository. Structural MRIs were acquired in ADNI-2 and ADNI-3 phases using 3T MRI scanners with 3D magnetization-prepared rapid gradient echo (MP-RAGE) or inversion recovery-fast spoiled gradient recalled (IR-SPGR) sequences. Detailed protocols of MRI scanner for T1-weighted imaging can be found online (http://adni.loni.usc.edu/methods/documents/mri-protocols/). Florbetapir PET scans were acquired for 20 minutes (4 × 5 min frames) at 50-70 min post injection of 10 mCi tracers, and Flortaucipir PET scans were acquired for 30 min (6 × 5 min frames) at 75-105 min post injection of 10 mCi tracers. We only used MRI scans having the shortest interval between MRI and Flortaucipir PET acquisition, all within six months (37 ± 40 days) of each other. Florbetapir images were used if acquired within 1 year of Flortaucipir (23 ± 38 days), in keeping with previous approaches (Das et al., 2018, Maass et al., 2017). DWI had the same acquisition date as the corresponding T1-weighted MRI. Multiple b=0 s/mm^2 images and 48 b=1000 s/mm^2 images were acquired for DWI with 2 × 2 ×2 mm^3 voxels in ADNI-3 phase (http://adni.loni.usc.edu/methods/). In the validation (Korean) dataset, T1-weighted MRI was also obtained using a 3T MR scanner with 3D SPGR sequence. Each of the Florbetaben and Flortaucipir PET scans was acquired for 20 minutes on separate days at 90 min and 80 minutes after the injection of tracers, respectively. Detailed acquisition parameters have been described (Cho et al., 2019).

PET image processing—Each Aβ- and tau-PET image for both baseline and follow-up scans was preprocessed as follows (Vogel et al., 2021). The raw PET image was first co-registered between frames to reduce motion effects with conversion to DICOM format and processed by averaging five-minute frames. The generated images were then reoriented into a standard 160 × 160 × 96 voxel image grid with 1.5 mm cubic voxels and intensity normalized. Finally, smoothing was performed with a scanner-specific filter function to make a uniform isotropic resolution of 8 mm full width at half maximum (Jagust et al., 2015) (http://adni.loni.usc.edu/). PET images were co-registered to the corresponding T1 image using FMRIB Software Library (FSL) Linear Registration Tool (FLIRT). For each hemisphere, we used the atlas parcellation comprising 105 cerebral cortical and 18 subcortical brain regions defined by the Brainnetome atlas (Fan et al., 2016), which was reverse-normalized to each participant's structural MRI scan. Standardized uptake value ratio (SUVR) images were obtained using whole cerebellum as a reference region. The

voxel values assigned to a previously identified region-of-interest (ROI) were averaged to obtain a regional SUVR value. The global retention ratio for Florbetapir images was computed based on Aβ-related regions including the frontal, anterior/posterior cingulate, lateral parietal, and lateral temporal regions (Jagust et al., 2015). Subjects were classified as amyloid-positive when the global Florbetapir retention ratio exceeded 1.11, consistent with previous approaches (Joshi et al., 2012) (http://adni.loni.usc.edu/).

Structural network construction—Structural networks were constructed using diffusion tensor imaging (DTI) techniques, based on eddy-current-corrected diffusion-weighted MR images (FSL, http://www.fmrib.ox.ac.uk/fsl/). Each structural network consisted of nodes (brain regions) and edges (connections between node pairs). For each hemisphere, the nodes comprised the 105 cerebral cortical and 18 subcortical brain regions defined by the Brainnetome atlas (Fan et al., 2016). T1-weighted MR image volumes from the Brainnetome atlas were resampled to corresponding eddy-current-corrected diffusion-weighted MR image volumes using FreeSurfer (http://surfer.nmr.mgh.harvard.edu/) to specify the nodes of each structural network. We derived the structural connectivity matrix at both individual and group levels. An individual-level network edge was deemed present if there was at least one streamline between a node pair, acquired by whole-brain deterministic tractography using the second order Runge-Kutta algorithm through the Diffusion toolkit (Wang et al., 2007). Fiber tracking was initiated at the 8 random points of each seed voxel with a fractional anisotropy (FA) > 0.3 and ended at the voxels with FA < 0.2 or a tract turning angle of > 45 degrees. The strength of each edge was determined based on the FA values averaged across all connecting streamlines using the UCLA Multimodal Connectivity Package (https://github.com/jbrown81/umcp) (van den Heuvel and Sporns, 2011). FA values have been considered to represent the level of microstructural organization of white matter tracts (Beaulieu, 2002), which has been associated with the functional efficacy of the connections (Ewing-Cobbs et al., 2006, Gold et al., 2007). The group-level network was computed by averaging individual network edges present in more than a third of all healthy (Aβ- CN) subjects. In the group-level network, 4.68% of edges were connected, and their range of mean FA values was 0.2215 [0.1766, 0.2842] (median [Q1, Q3]).

Quantification and statistical analysis

Determination of individual tau-PET pattern—We employed gaussian mixture modeling for each ROI to address off-target Flortaucipir binding (Choi et al., 2018, Lemoine et al., 2018, Lockhart et al., 2017). Following previous approaches (Vogel et al., 2020), we assumed that a distribution of pathological signal would be skewed while those of off-target and non-specific signals would remain normally distributed across the study sample. All Flortaucipir SUVR values of each ROI were fitted through a one-component and a two-component gaussian mixture model, of which the results were compared five times using Bayesian information criterion (BIC). Consistently lower BIC in a one-component model than a two-component model indicates SUVR values of the region are roughly normally distributed, implying no evidence of pathological tau deposition. The regions fitted better with a one-component model were considered as not or not yet involved in tauopathy, so not included in the study (33 brain regions were regarded as off-target regions for the ADNI dataset and 46 for the Korean validation dataset (see Table S2)).

We then constructed a *W*-score map (Jack et al., 1997, La Joie et al., 2012, Ossenkoppele et al., 2015) for each Flortaucipir PET image to represent individual pathological tau burden compared to the amyloid-PET-negative CN group (Tsai et al., 2019). *W*-scores are standardized values adjusted for covariates including age, sex, and years of education. For each ROI, a linear regression was performed between the covariates and the regional SUVR values in the control group. The *W*-score was computed as a difference between actual and predicted pathological burden (i.e. the residual) of each subject, divided by the standard deviation of residuals in the control group. In the individual *W*-score maps generated for Flortaucipir PET scans, greater values indicate greater Flortaucipir uptake, suggesting greater tau pathological burden.

Determination of pseudo-longitudinal order—To study the non-linear acceleration of tau aggregation required the use of cross-sectional data to make longitudinal inferences. To this end, we first constructed a pseudo-longitudinal order by applying a frequency-based method to the tau-PET data of presymptomatic and prodromal AD (Aβ-positive CN and MCI, early or late) subjects. ROIs were ordered to define a regional tau spreading order by the frequencies with which the regional *W*-scores exceeded a given threshold across all subjects. We used a *W*-score threshold of 2.5, following previous research (Cho et al., 2016), but other thresholds were also considered to evaluate robustness (see Figure S1). Subjects were sorted based on their number of ROIs having suprathreshold tau *W*-scores. To determine the period in which tau acceleration occurs, we used a smoothed line of the frequency graph based on the pseudo-longitudinal order. We deemed that the acceleration phase begins where the slope of the graph becomes larger than two and ends at the second inflection point, where the second derivative become zero.

Network flow-based connectivity derivation—We constructed a flow-based network based on maximum inter-nodal flow, using the whole-brain structural network to model the extent of tau propagation between each node pair. Every possible non-overlapping distinct path between any two nodes was extracted by employing a graph-theoretical maximum-flow calculation method using the binary normative brain network (Wook Yoo et al., 2015, Wilson, 1979). Each separate path contributed to the total inter-nodal flow by the amount of the mean FA value of all edges in the path divided by the average inter-nodal streamline length in mm. The partial contributions were then combined through all distinct paths, which became an edge weight between the source and sink nodes in the flow-based connectivity matrix. By adopting multiple distinct paths between two nodes, the flow-based network provides a method for predicting the physical amount of tau delivered from the source to sink node. This flow network was constructed at both the individual and group levels using the healthy structural connectome.

Propagation hub identification—The flow-based network described above was next used to identify propagation hubs, hypothesized to drive the acceleration phase of tau spreading. To this end, we searched a library of network flow-based connectivity maps, one seeded by each of the 246 brain regions-of-interest, and we estimated the goodness-of-fit (GOF) of each seed's map to the progression of tau through the regions representing the tau acceleration phase. Specifically, binary inner and outer masks were defined within the tau

acceleration phase regions across a range of thresholds (see Figure S3). Assuming that the propagation hubs template the topography of acceleration phase tau spreading, the inner and outer mask regions were constrained to tau acceleration phase regions, arranged using the pseudo-longitudinal regional tau spreading order. We assigned the first thirty brain regions to the inner mask and the next thirty regions to the outer mask to capture earlier and later tau spreading. The inner mask was then gradually expanded by ten regions, producing 7 different sets of inner-outer mask pairs (see Figure S3), to mimic tau propagation and to avoid potential influence of arbitrary thresholding. For example, the second mask set had the first forty regions as the inner mask and the next thirty regions as the outer mask. A GOF score was calculated for each seed by subtracting its average connectivity to the outer mask area from its average connectivity to the inner mask area., and a permutation-based one-sample t-test was performed using the GOF scores. The significance level was determined using $p < 0.05$, Bonferroni-corrected for multiple tests. The propagation hubs were identified as the regions showing significant GOF scores for all 7 mask pairs. In this way, regions that show the highest and most robust connectivity to regions that become tau-positive early in the acceleration phase were selected as propagation hubs.

Statistical evaluation of network spread—To assess the relationship between the network flow-based connectivity in health and the topographical pattern of tau acceleration phase, we performed correlation analyses between the group-level flow network derived from the identified ITG propagation hubs and the group-level tau-PET *W*-score contrast maps from ADNI subjects. The tau-PET contrast map was obtained by averaging all possible two-subject tau-PET *W*-score difference maps from subjects drawn (one each) from the acceleration and pre-acceleration periods. The pre-acceleration period consists of subjects ordered before the acceleration phase, based on the pseudo-longitudinal subject order, insofar as they had at least one tau-positive region. Correlations were then evaluated in each hemisphere using the ipsilateral propagation hub. To place our findings in context of previous work from our group (Brown et al., 2019, Zhou et al., 2012), we compared the network flow-based correlations to those derived using shortest path length and Euclidean distance from the propagation hubs. The matrix of shortest path length was computed using group-level FA-weighted structural connectivity, and the Euclidean distances between each pair of nodes were averaged through all healthy subjects. For the correlation analyses, statistical significance was set to $p < 0.05$ and multiple comparisons were corrected using the Benjamini-Hochberg false discovery rate (FDR) method (Benjamini and Hochberg, 1995) across three different measures and the two ITG propagation hubs. Furthermore, we calculated the null distribution of z-transformed correlation coefficients using all brain regions as seeds to assess the statistical meaning of the correlation coefficient for the ITG propagation hubs compared to other regions in terms of correlation with the topographical tau deposition representing the acceleration > pre-acceleration phase pattern as defined above.

Analysis of network-based Aβ-tau interactions—We evaluated the relationship between Aβ and tau based on remote and local interactions. For computing remote interactions of each ROI, Aβ-PET SUVR values in each connected region, based on the structural connectome, were multiplied by the FA value of the connecting tract, inversely

weighted by the streamline length, based on the notion that remote interactions will reflect the strength of the connection and the distance over which these effects must travel (Iturria-Medina et al., 2014, Waters, 2010). The connectivity-weighted Aβ-PET SUVRs for all connected regions were summed, and this remote Aβ influence value was then multiplied by the tau *W*-score of the ROI. In this way, a region's remote Aβ-tau interaction was determined by the strength and number of its connections to Aβ-PET-positive brain areas and by its local tau deposition. Similarly, local Aβ-tau interactions were obtained by multiplying the region's Aβ-PET SUVR by the region's local tau *W*-score. For the magnitude of Aβ deposition, the regional Aβ-PET SUVR value was used because of its narrow dynamic range; in this context, *W*-score normalization may skew or exaggerate small changes in Aβ deposition (Grothe et al., 2017).

To estimate where the remote and local interactions take place earliest in AD progression, we applied the same frequency-based method used for constructing the pseudo-longitudinal tau spreading order. Brain regions were ordered using the frequencies with which their remote or local Aβ influence metric was positive and the tau *W*-score exceeded a given threshold. Both remote Aβ influence and local Aβ positivity were determined using regional cutoff values calculated by employing a previously reported method (Aizenstein et al., 2008) that iteratively removes outliers within each region's data from the Aβ-negative CN group until no outlier arises and multiplies the maximum of remaining values by a small number as a buffer. We considered the values higher than 1.5 × the interquartile range over the third quartile as outliers and identified a cutoff value as the 95^{th} percentile value of the remaining data after removing outliers. In addition, we compared the interaction score of each region with the median interaction scores of all other regions from the ipsilateral hemisphere. For this comparison, the continuous values of both interaction scores were used. To address regional variations in Aβ-PET SUVR across the whole brain, we normalized the remote/local Aβ influence using the regional cutoffs, which were multiplied by each ROI's local tau *W*-score to compute the remote and local Aβ-tau interaction scores. Permutation-based one-sample t-tests were used across all subjects and multiple comparisons were corrected using the FDR method(Benjamini and Hochberg, 1995) across all regions within each hemisphere. To verify robustness of the interaction pseudo-order, we also considered a range of tau thresholds (see Figure S6).

According to our hypotheses and main results (see Figure 4), we assumed that the remote Aβ-tau interactions occur earliest in the entorhinal cortex and have a critical influence on tau spreading from the EC, whereas local interactions occur early and crucially within the ITG. Therefore, we examined the location of the EC on the distribution of t-statistics for remote interaction scores and the inferior temporal gyrus on the distribution of t-statistics for local interaction scores (see Figures 4 and S7).

Longitudinal analyses of tau acceleration—To strengthen the statistical power of the longitudinal analyses, we used regional tau *W*-scores of the ADNI and Korean datasets together. First, to determine whether the connectivity of the ITG stands out as a predictor of longitudinal tau accumulation, we performed correlation analyses between the regional flow-based networks, derived from healthy controls, and the group-level annualized change in tau-PET *W*-maps, derived from Aβ+ subjects with MCI (n = 68). Off-target regions

co-occurring in both datasets were removed from the correlation analyses but retained in network flow-based map construction, in keeping with the cross-sectional analyses. The correlation coefficients of all seed regions were transformed to z-scores, and the values of the ITG propagation hubs were presented on the distribution (see Figure 5A).

Next, to assess the relationship between the two key Aβ-tau interactions and longitudinal tau accumulation, subjects were stratified by the status of local Aβ and tau for each ROI separately (including both left and right EC and ITG) as follows: (1) both Aβ and tau were negative (−/−), (2) Aβ was positive while tau was negative (+/−), (3) Aβ was negative while tau was positive (−/+), and (4) both were positive (+/+). Necessarily, for each region-of-interest, groups 1-4 had different subject compositions. For each subject, we determined the tau accumulation rate in regions "downstream" to the region-of-interest, by averaging the annualized change rates across tau *W*-scores among the 30 regions immediately following the region-of-interest within the dataset-specific regional tau spreading order. We first performed two-sample t-tests using the averaged annualized change rates to compare the effects of the EC being Aβ-positive vs. Aβ-negative in the presence of local tau-positivity. For the EC, subjects with negative local Aβ and positive tau were further divided into two subgroups according to the EC remote Aβ-tau interaction status: remote Aβ-negative/local tau-positive and remote Aβ-positive/local tau-positive (see Figure 5B). The downstream tau accumulation rates of the two subgroups were compared to examine the effects of remote Aβ on tau within the EC, using a Mann-Whitney U test, appropriate here due to the nonparametric distribution of the tau accumulation rate in these subgroups. We next evaluated the effects of local interaction between Aβ and tau within the ITG (Figure 5C). Subjects lacking local tau while having positive Aβ within the ITG were further divided into two sub-groups based on whether tau positivity emerged in the ITG at follow-up. The rationale for this subgrouping was that it would allow us to determine whether arrival of tau at the (already Aβ-positive) ITG promoted greater downstream tau spreading. We then compared these subgroups using a Mann-Whitney U test. The number of downstream regions assessed in these analyses was first set to 30, but we also addressed effects over a range of this parameter from 20 to 50 (see Table S6).

Network model-based subject stratification—Our findings suggested two important transitions during the natural history of AD, based on: (1) remote Aβ-tau interaction within the lateral EC and (2) local Aβ-tau interaction within the ITG. To examine subjects' status with respect to these transitions, we computed quantitative thresholds for each metric. The first threshold was computed by multiplying the regional cutoff of the EC remote Aβ influence metric by the tau *W*-score cutoff (2.5 in our study). Similarly, for the second threshold, the regional cutoff for the ITG local amyloid SUVR was multiplied by the tau *W*-score cutoff. Using this approach, we classified each subject into one of four groups: (1) least affected by the tau pathology ("tau-negative") in EC (Baek et al., 2020), (2) subthreshold EC remote Aβ-tau interaction despite the presence of EC tau ("latent tau" group), (3) suprathreshold EC remote Aβ-tau interaction but subthreshold ITG Aβ-tau local interaction ("spreading tau" group), and (4) suprathreshold ITG Aβ-tau local interaction ("propagating tau" group). Values for each metric were calculated in each hemisphere separately. Subjects were assigned to the latent tau group if they had subthreshold values in

both hemispheres for Threshold 1, whereas they were stratified to the propagating tau group if they had suprathreshold values in both hemispheres for Threshold 2. If one hemisphere would yield assignment to the latent tau and the other to propagating tau group, then the subject was assigned to the latent tau group, based on the notion that they might, upon re-testing, move into the spreading tau group as defined.

Supplementary Material

Refer to Web version on PubMed Central for supplementary material.

Acknowledgements

Data collection and sharing for this project was funded by the Alzheimer's Disease Neuroimaging Initiative (ADNI) (National Institutes of Health Grant U01 AG024904) and DOD ADNI (Department of Defense award number W81XWH-12-2-0012). ADNI is funded by the National Institute on Aging, the National Institute of Biomedical Imaging and Bioengineering, and through generous contributions from the following: AbbVie, Alzheimer's Association; Alzheimer's Drug Discovery Foundation; Araclon Biotech; BioClinica, Inc.; Biogen; Bristol-Myers Squibb Company; CereSpir, Inc.; Cogstate; Eisai Inc.; Elan Pharmaceuticals, Inc.; Eli Lilly and Company; EuroImmun; F. Hoffmann-La Roche Ltd and its affiliated company Genentech, Inc.; Fujirebio; GE Healthcare; IXICO Ltd.; Janssen Alzheimer Immunotherapy Research & Development, LLC.; Johnson & Johnson Pharmaceutical Research & Development LLC.; Lumosity; Lundbeck; Merck & Co., Inc.; Meso Scale Diagnostics, LLC.; NeuroRx Research; Neurotrack Technologies; Novartis Pharmaceuticals Corporation; Pfizer Inc.; Piramal Imaging; Servier; Takeda Pharmaceutical Company; and Transition Therapeutics. The Canadian Institutes of Health Research is providing funds to support ADNI clinical sites in Canada. Private sector contributions are facilitated by the Foundation for the National Institutes of Health (www.fnih.org). The grantee organization is the Northern California Institute for Research and Education, and the study is coordinated by the Alzheimer's Therapeutic Research Institute at the University of Southern California. ADNI data are disseminated by the Laboratory for Neuro Imaging at the University of Southern California.

This work was partly supported by the National Research Foundation of Korea (NRF) grant funded by the Korea government (MSIP) (No. 2019R1A2C109021211, NRF2020R1F1A1076154, NRF2020R1C1C1014725 & NRF2018R1D1A1B07049386),Yonsei University College of Medicine grant 6-2021-0094, the Institute of Information & communications Technology Planning & Evaluation (IITP) grant funded by the Korea government (MSIT) (No. 2019-0-00079, Department of Artificial Intelligence (Korea University)), Korea Health Industry Development Institute (HU20C0164), and by NIH grants AG019724, AG062422, AG055698, and AG065501.

References

AIZENSTEIN HJ, NEBES RD, SAXTON JA, PRICE JC, MATHIS CA, TSOPELAS ND, ZIOLKO SK, JAMES JA, SNITZ BE, HOUCK PR, BI W, COHEN AD, LOPRESTI BJ, DEKOSKY ST, HALLIGAN EM & KLUNK WE 2008. Frequent Amyloid Deposition Without Significant Cognitive Impairment Among the Elderly. Archives of Neurology, 65, 1509–1517. [PubMed: 19001171]

ALBERT MS, DEKOSKY ST, DICKSON D, DUBOIS B, FELDMAN HH, FOX NC, GAMST A, HOLTZMAN DM, JAGUST WJ, PETERSEN RC, SNYDER PJ, CARRILLO MC, THIES B & PHELPS CH 2011. The diagnosis of mild cognitive impairment due to Alzheimer's disease: Recommendations from the National Institute on Aging-Alzheimer's Association workgroups on diagnostic guidelines for Alzheimer's disease. Alzheimer's & Dementia, 7, 270–279.

BAEK MS, CHO H, LEE HS, CHOI JY, LEE JH, RYU YH, LEE MS & LYOO CH 2020. Temporal trajectories of in vivo tau and amyloid-β accumulation in Alzheimer's disease. European Journal of Nuclear Medicine and Molecular Imaging, 47, 2879–2886. [PubMed: 32350558]

BEAULIEU C 2002. The basis of anisotropic water diffusion in the nervous system – a technical review. NMR in Biomedicine, 15, 435–455. [PubMed: 12489094]

BENJAMINI Y & HOCHBERG Y 1995. Controlling the False Discovery Rate: A Practical and Powerful Approach to Multiple Testing. Journal of the Royal Statistical Society. Series B (Methodological), 57, 289–300.

BRAAK H, ALAFUZOFF I, ARZBERGER T, KRETZSCHMAR H & DEL TREDICI K 2006. Staging of Alzheimer disease-associated neurofibrillary pathology using paraffin sections and immunocytochemistry. Acta Neuropathologica, 112, 389–404. [PubMed: 16906426]

BRAAK H & BRAAK E 1991. Neuropathological staging of Alzheimer-related changes. Acta Neuropathologica, 82, 239–259. [PubMed: 1759558]

BRAAK H & DEL TREDICI K 2011. Alzheimer's pathogenesis: is there neuron-to-neuron propagation? Acta Neuropathologica, 121, 589–95. [PubMed: 21516512]

BROWN JA, DENG J, NEUHAUS J, SIBLE IJ, SIAS AC, LEE SE, KORNAK J, MARX GA, KARYDAS AM, SPINA S, GRINBERG LT, COPPOLA G, GESCHWIND DH, KRAMER JH, GORNO-TEMPINI ML, MILLER BL, ROSEN HJ & SEELEY WW 2019. Patient-Tailored, Connectivity-Based Forecasts of Spreading Brain Atrophy. Neuron, 104, 856–868.e5. [PubMed: 31623919]

CHO H, CHOI JY, HWANG MS, KIM YJ, LEE HM, LEE HS, LEE JH, RYU YH, LEE MS & LYOO CH 2016. In vivo cortical spreading pattern of tau and amyloid in the Alzheimer disease spectrum. Annals of Neurology, 80, 247–258. [PubMed: 27323247]

CHO H, CHOI JY, LEE HS, LEE JH, RYU YH, LEE MS, JACK CR & LYOO CH 2019. Progressive Tau Accumulation in Alzheimer Disease: 2-Year Follow-up Study. Journal of Nuclear Medicine, 60, 1611–1621. [PubMed: 30926651]

CHOI JY, CHO H, AHN SJ, LEE JH, RYU YH, LEE MS & LYOO CH 2018. Off-Target 18F-AV-1451 Binding in the Basal Ganglia Correlates with Age-Related Iron Accumulation. Journal of Nuclear Medicine, 59, 117–120. [PubMed: 28775201]

CLAVAGUERA F, AKATSU H, FRASER G, CROWTHER RA, FRANK S, HENCH J, PROBST A, WINKLER DT, REICHWALD J, STAUFENBIEL M, GHETTI B, GOEDERT M & TOLNAY M 2013. Brain homogenates from human tauopathies induce tau inclusions in mouse brain. Proc Natl Acad Sci U S A, 110, 9535–40. [PubMed: 23690619]

CRARY JF, TROJANOWSKI JQ, SCHNEIDER JA, ABISAMBRA JF, ABNER EL, ALAFUZOFF I, ARNOLD SE, ATTEMS J, BEACH TG, BIGIO EH, CAIRNS NJ, DICKSON DW, GEARING M, GRINBERG LT, HOF PR, HYMAN BT, JELLINGER K, JICHA GA, KOVACS GG, KNOPMAN DS, KOFLER J, KUKULL WA, MACKENZIE IR, MASLIAH E, MCKEE A, MONTINE TJ, MURRAY ME, NELTNER JH, SANTA-MARIA I, SEELEY WW, SERRANO-POZO A, SHELANSKI ML, STEIN T, TAKAO M, THAL DR, TOLEDO JB, TRONCOSO JC, VONSATTEL JP, WHITE CL 3RD, WISNIEWSKI T, WOLTJER RL, YAMADA M & NELSON PT 2014. Primary age-related tauopathy (PART):a common pathology associated with human aging. Acta neuropathologica, 128, 755–766. [PubMed: 25348064]

CUMMINGS J & SALLOWAY S 2021. Aducanumab: Appropriate use recommendations. Alzheimer's & Dementia, n/a.

DAS SR, XIE L, WISSE LEM, ITTYERAH R, TUSTISON NJ, DICKERSON BC, YUSHKEVICH PA & WOLK DA 2018. Longitudinal and cross-sectional structural magnetic resonance imaging correlates of AV-1451 uptake. Neurobiology of Aging, 66, 49–58. [PubMed: 29518752]

EWING-COBBS L, HASAN KM, PRASAD MR, KRAMER L & BACHEVALIER J 2006. Corpus callosum diffusion anisotropy correlates with neuropsychological outcomes in twins disconcordant for traumatic brain injury. AJNR. American journal of neuroradiology, 27, 879–881. [PubMed: 16611782]

FAN L, LI H, ZHUO J, ZHANG Y, WANG J, CHEN L, YANG Z, CHU C, XIE S, LAIRD AR, FOX PT, EICKHOFF SB, YU C & JIANG T 2016. The Human Brainnetome Atlas: A New Brain Atlas Based on Connectional Architecture. Cerebral Cortex, 26, 3508–3526. [PubMed: 27230218]

FRANZMEIER N, NEITZEL J, RUBINSKI A, SMITH R, STRANDBERG O, OSSENKOPPELE R, HANSSON O, EWERS M & ALZHEIMER'S DISEASE NEUROIMAGING I. 2020. Functional brain architecture is associated with the rate of tau accumulation in Alzheimer's disease. Nat Commun, 11, 347. [PubMed: 31953405]

GOLD BT, POWELL DK, XUAN L, JIANG Y & HARDY PA 2007. Speed of lexical decision correlates with diffusion anisotropy in left parietal and frontal white matter: evidence from diffusion tensor imaging. Neuropsychologia, 45, 2439–2446. [PubMed: 17509627]

GROTHE MJ, BARTHEL H, SEPULCRE J, DYRBA M, SABRI O & TEIPEL SJ 2017. In vivo staging of regional amyloid deposition. Neurology, 89, 2031. [PubMed: 29046362]

HE Z, GUO JL, MCBRIDE JD, NARASIMHAN S, KIM H, CHANGOLKAR L, ZHANG B, GATHAGAN RJ, YUE C, DENGLER C, STIEBER A, NITLA M, COULTER DA, ABEL T, BRUNDEN KR, TROJANOWSKI JQ & LEE VM 2018. Amyloid-beta plaques enhance Alzheimer's brain tau-seeded pathologies by facilitating neuritic plaque tau aggregation. Nat Med, 24, 29–38. [PubMed: 29200205]

HOAGLIN DC, MOSTELLER F & TUKEY JW 2000. Understanding robust and exploratory data analysis.

HYMAN BT, DAMASIO AR, VAN HOESEN GW & BARNES CL 1984. Alzheimer's disease: cell-specific pathology isolates the hippocampal formation. Science, 298, 83–95.

INDRAYAN A & MALHOTRA RK 2017. Medical biostatistics, CRC Press.

ITURRIA-MEDINA Y, SOTERO RC, TOUSSAINT PJ, EVANS AC & ALZHEIMER'S DISEASE NEUROIMAGING, I. 2014. Epidemic spreading model to characterize misfolded proteins propagation in aging and associated neurodegenerative disorders. PLoS computational biology, 10, e1003956–e1003956. [PubMed: 25412207]

JACK CR, KNOPMAN DS, JAGUST WJ, SHAW LM, AISEN PS, WEINER MW, PETERSEN RC & TROJANOWSKI JQ 2010. Hypothetical model of dynamic biomarkers of the Alzheimer's pathological cascade. The Lancet Neurology, 9, 119–128. [PubMed: 20083042]

JACK CR, PETERSEN RC, XU YC, WARING SC, O'BRIEN PC, TANGALOS EG, SMITH GE, IVNIK RJ & KOKMEN E 1997. Medial temporal atrophy on MRI in normal aging and very mild Alzheimer's disease. Neurology, 49, 786–794. [PubMed: 9305341]

JAGUST W 2018. Imaging the evolution and pathophysiology of Alzheimer disease. Nature Reviews Neuroscience, 19, 687–700. [PubMed: 30266970]

JAGUST WJ, LANDAU SM, KOEPPE RA, REIMAN EM, CHEN K, MATHIS CA, PRICE JC, FOSTER NL & WANG AY 2015. The Alzheimer's Disease Neuroimaging Initiative 2 PET Core: 2015. Alzheimer's & dementia : the journal of the Alzheimer's Association, 11, 757–771.

JOHNSON KA, SCHULTZ A, BETENSKY RA, BECKER JA, SEPULCRE J, RENTZ D, MORMINO E, CHHATWAL J, AMARIGLIO R, PAPP K, MARSHALL G, ALBERS M, MAURO S, PEPIN L, ALVERIO J, JUDGE K, PHILIOSSAINT M, SHOUP T, YOKELL D, DICKERSON B, GOMEZ-ISLA T, HYMAN B, VASDEV N & SPERLING R 2016. Tau positron emission tomographic imaging in aging and early Alzheimer disease. Annals of Neurology, 79, 110–119. [PubMed: 26505746]

JOSHI AD, PONTECORVO MJ, CLARK CM, CARPENTER AP, JENNINGS DL, SADOWSKY CH, ADLER LP, KOVNAT KD, SEIBYL JP, ARORA A, SAHA K, BURNS JD, LOWREY MJ, MINTUN MA, SKOVRONSKY DM & INVESTIGATORS T. F. F. S. 2012. Performance Characteristics of Amyloid PET with Florbetapir F 18 in Patients with Alzheimer's Disease and Cognitively Normal Subjects. 53, 378–384.

KIM EJ, HWANG JL, GAUS SE, NANA AL, DENG J, BROWN JA, SPINA S, LEE MJ, RAMOS EM, GRINBERG LT, KRAMER JH, BOXER AL, GORNO-TEMPINI ML, ROSEN HJ, MILLER BL & SEELEY WW 2019. Evidence of corticofugal tau spreading in patients with frontotemporal dementia. Acta Neuropathol.

LA JOIE R, PERROTIN A, BARRë L, HOMMET C, MëZENGE F, IBAZIZENE M, CAMUS V, ABBAS A, LANDEAU B & GUILLOTEAU D 2012. Region-specific hierarchy between atrophy, hypometabolism, and β-amyloid (Aβ) load in Alzheimer's disease dementia. Journal of Neuroscience, 32, 16265–16273. [PubMed: 23152610]

LEMOINE L, LEUZY A, CHIOTIS K, RODRIGUEZ-VIEITEZ E & NORDBERG A2018. Tau positron emission tomography imaging in tauopathies: The added hurdle of off-target binding. Alzheimer's & Dementia: Diagnosis, Assessment & Disease Monitoring, 10,232–236.

LEUZY A, CHIOTIS K, LEMOINE L, GILLBERG P-G, ALMKVIST O, RODRIGUEZ-VIEITEZ E & NORDBERG A 2019. Tau PET imaging in neurodegenerative tauopathies—still a challenge. Molecular Psychiatry, 24, 1112–1134. [PubMed: 30635637]

LIU L, DROUET V, WU JW, WITTER MP, SMALL SA, CLELLAND C & DUFF K 2012. Trans-synaptic spread of tau pathology in vivo. PLoS One, 7, e31302. [PubMed: 22312444]

LOCKHART SN, AYAKTA N, WINER JR, LA JOIE R, RABINOVICI GD & JAGUST WJ 2017. Elevated (18)F-AV-1451 PET tracer uptake detected in incidental imaging findings. Neurology, 88, 1095–1097. [PubMed: 28188303]

MAASS A, LANDAU S, BAKER SL, HORNG A, LOCKHART SN, LA JOIE R, RABINOVICI GD & JAGUST WJ 2017. Comparison of multiple tau-PET measures as biomarkers in aging and Alzheimer's disease. NeuroImage, 157, 448–463. [PubMed: 28587897]

MAIER-HEIN KH, NEHER PF, HOUDE J-C, CöTë M-A, GARYFALLIDIS E, ZHONG J, CHAMBERLAND M, YEH F-C, LIN Y-C, JI Q, REDDICK WE, GLASS JO, CHEN DQ, FENG Y, GAO C, WU Y, MA J, HE R, LI Q, WESTIN C-F, DESLAURIERS-GAUTHIER S, GONZãLEZ JOO, PAQUETTE M, ST-JEAN S, GIRARD G, RHEAULT F, SIDHU J, TAX CMW, GUO F, MESRI HY, DãVID S, FROELING M, HEEMSKERK AM, LEEMANS A, BORë A, PINSARD B, BEDETTI C, DESROSIERS M, BRAMBATI S, DOYON J, SARICA A, VASTA R, CERASA A, QUATTRONE A, YEATMAN J, KHAN AR, HODGES W, ALEXANDER S, ROMASCANO D, BARAKOVIC M, AURïA A, ESTEBAN O, LEMKADDEM A, THIRAN J-P, CETINGUL HE, ODRY BL, MAILHE B, NADAR MS, PIZZAGALLI F, PRASAD G, VILLALON-REINA JE, GALVIS J, THOMPSON PM, REQUEJO FDS, LAGUNA PL, LACERDA LM, BARRETT R, DELL'ACQUA F, CATANI M, PETIT L, CARUYER E, DADUCCI A, DYRBY TB, HOLLAND-LETZ T, HILGETAG CC, STIELTJES B & DESCOTEAUX M 2017. The challenge of mapping the human connectome based on diffusion tractography. Nature Communications, 8, 1349.

MCDADE E, WANG G, GORDON BA, HASSENSTAB J, BENZINGER TLS, BUCKLES V, FAGAN AM, HOLTZMAN DM, CAIRNS NJ, GOATE AM, MARCUS DS, MORRIS JC, PAUMIER K, XIONG C, ALLEGRI R, BERMAN SB, KLUNK W, NOBLE J, RINGMAN J, GHETTI B, FARLOW M, SPERLING RA, CHHATWAL J, SALLOWAY S, GRAFF-RADFORD NR, SCHOFIELD PR, MASTERS C, ROSSOR MN, FOX NC, LEVIN J, JUCKER M, BATEMAN RJ & DOMINANTLY INHERITED ALZHEIMER N 2018. Longitudinal cognitive and biomarker changes in dominantly inherited Alzheimer disease. Neurology, 91, e1295–e1306. [PubMed: 30217935]

MCKHANN GM, KNOPMAN DS, CHERTKOW H, HYMAN BT, JACK CR, KAWAS CH, KLUNK WE, KOROSHETZ WJ, MANLY JJ, MAYEUX R, MOHS RC, MORRIS JC, ROSSOR MN, SCHELTENS P, CARRILLO MC, THIES B, WEINTRAUB S & PHELPS CH 2011. The diagnosis of dementia due to Alzheimer's disease: Recommendations from the National Institute on Aging-Alzheimer's Association workgroups on diagnostic guidelines for Alzheimer's disease. Alzheimer's & Dementia, 7, 263–269.

MINTUN MA, LO AC, DUGGAN EVANS C, WESSELS AM, ARDAYFIO PA, ANDERSEN SW, SHCHERBININ S, SPARKS J, SIMS JR, BRYS M, APOSTOLOVA LG, SALLOWAY SP & SKOVRONSKY DM 2021. Donanemab in Early Alzheimer's Disease. New England Journal of Medicine, 384, 1691–1704. [PubMed: 33720637]

MUSIEK ES & HOLTZMAN DM 2012. Origins of Alzheimer's disease: reconciling cerebrospinal fluid biomarker and neuropathology data regarding the temporal sequence of amyloid-beta and tau involvement. Current Opinion in Neurology, 25, 715–20. [PubMed: 23041958]

OSSENKOPPELE R, IACCARINO L, SCHONHAUT DR, BROWN JA, LA JOIE R, O'NEIL JP, JANABI M, BAKER SL, KRAMER JH, GORNO-TEMPINI ML, MILLER BL, ROSEN HJ, SEELEY WW, JAGUST WJ & RABINOVICI GD 2019. Tau covariance patterns in Alzheimer's disease patients match intrinsic connectivity networks in the healthy brain. Nenroimage Clin, 23, 101848.

OSSENKOPPELE R, PIJNENBURG YA, PERRY DC, COHN-SHEEHY BI, SCHELTENS NM, VOGEL JW, KRAMER JH, VAN DER VLIES AE, JOIE RL & ROSEN HJ 2015. The behavioural/dysexecutive variant of Alzheimer's disease: clinical, neuroimaging and pathological features. Brain, 138, 2732–2749. [PubMed: 26141491]

PETERSEN RC, AISEN PS, BECKETT LA, DONOHUE MC, GAMST AC, HARVEY DJ, JACK CR JR., JAGUST WJ, SHAW LM, TOGA AW, TROJANOWSKI JQ & WEINER MW 2010. Alzheimer's Disease Neuroimaging Initiative (ADNI): clinical characterization. Neurology, 74, 201–209. [PubMed: 20042704]

RAJ A, KUCEYESKI A & WEINER M 2012. A Network Diffusion Model of Disease Progression in Dementia. Neuron, 73, 1204–1215. [PubMed: 22445347]

RAJ A, LOCASTRO E, KUCEYESKI A, TOSUN D, RELKIN N, WEINER M & FOR THE ALZHEIMER'S DISEASE NEUROIMAGING, I. 2015. Network Diffusion Model of Progression Predicts Longitudinal Patterns of Atrophy and Metabolism in Alzheimer's Disease. Cell Rep.

SANCHEZ JS, BECKER JA, JACOBS HIL, HANSEEUW BJ, JIANG S, SCHULTZ AP, PROPERZI MJ, KATZ SR, BEISER A, SATIZABAL CL, O'DONNELL A, DECARLI C, KILLIANY R, EL FAKHRI G, NORMANDIN MD, GõMEZ-ISLA T, QUIROZ YT, RENTZ DM, SPERLING RA, SESHADRI S, AUGUSTINACK J, PRICE JC & JOHNSON KA 2021a. The cortical origin and initial spread of medial temporal tauopathy in Alzheimer's disease assessed with positron emission tomography. Science Translational Medicine, 13, eabc0655. [PubMed: 33472953]

SANCHEZ JS, HANSEEUW BJ, LOPERA F, SPERLING RA, BAENA A, BOCANEGRA Y, AGUILLON D, GUZMãN-VëLEZ E, PARDILLA-DELGADO E, RAMIREZ-GOMEZ L, VILA-CASTELAR C, MARTINEZ JE, FOX-FULLER JT, RAMOS C, OCHOA-ESCUDERO M, ALVAREZ S, JACOBS HIL, SCHULTZ AP, GATCHEL JR, BECKER JA, KATZ SR, MAYBLYUM DV, PRICE JC, REIMAN EM, JOHNSON KA & QUIROZ YT 2021b. Longitudinal amyloid and tau accumulation in autosomal dominant Alzheimer's disease: findings from the Colombia-Boston (COLBOS) biomarker study. Alzheimer's Research & Therapy, 13, 27.

SCOTT MR, HAMPTON OL, BUCKLEY RF, CHHATWAL JP, HANSEEUW BJ, JACOBS HIL, PROPERZI MJ, SANCHEZ JS, JOHNSON KA, SPERLING RA & SCHULTZ AP 2020. Inferior temporal tau is associated with accelerated prospective cortical thinning in clinically normal older adults. NeuroImage, 220, 116991. [PubMed: 32512123]

SEPULCRE J, GROTHE MJ, D'OLEIRE UQUILLAS F, ORTIZ-TERAN L, DIEZ I, YANG HS, JACOBS HIL, HANSEEUW BJ, LI Q, EL-FAKHRI G, SPERLING RA & JOHNSON KA 2018. Neurogenetic contributions to amyloid beta and tau spreading in the human cortex. Nat Med, 24, 1910–1918. [PubMed: 30374196]

THAL DR, RþB U, ORANTES M & BRAAK H 2002. Phases of A beta-deposition in the human brain and its relevance for the development of AD. Neurology, 58, 1791–800. [PubMed: 12084879]

TSAI RM, BEJANIN A, LESMAN-SEGEV O, LAJOIE R, VISANI A, BOURAKOVA V, O'NEIL JP, JANABI M, BAKER S, LEE SE, PERRY DC, BAJOREK L, KARYDAS A, SPINA S, GRINBERG LT, SEELEY WW, RAMOS EM, COPPOLA G, GORNO-TEMPINI ML, MILLER BL, ROSEN HJ, JAGUST W, BOXER AL & RABINOVICI GD 2019. 18F-flortaucipir (AV-1451) tau PET in frontotemporal dementia syndromes. Alzheimer's Research & Therapy, 11, 13.

VAN DEN HEUVEL MP & SPORNS O 2011. Rich-Club Organization of the Human Connectome. The Journal of Neuroscience, 31, 15775. [PubMed: 22049421]

VOGEL JW, ITURRIA-MEDINA Y, STRANDBERG OT, SMITH R, LEVITIS E, EVANS AC, HANSSON O, ALZHEIMER'S DISEASE NEUROIMAGING I. & SWEDISH BIOFINDER S 2020. Spread of pathological tau proteins through communicating neurons in human Alzheimer's disease. Nat Commun, 11, 2612. [PubMed: 32457389]

VOGEL JW, YOUNG AL, OXTOBY NP, SMITH R, OSSENKOPPELE R, STRANDBERG OT, LA JOIE R, AKSMAN LM, GROTHE MJ, ITURRIA-MEDINA Y, WEINER M, AISEN P, PETERSEN R, JACK CR, JAGUST W, TROJANOWKI JQ, TOGA AW, BECKETT L, GREEN RC, SAYKIN AJ, MORRIS J, SHAW LM, LIU E, MONTINE T, THOMAS RG, DONOHUE M, WALTER S, GESSERT D, SATHER T, JIMINEZ G, HARVEY D, BERNSTEIN M, FOX N, THOMPSON P, SCHUFF N, DECARLI C, BOROWSKI B, GUNTER J, SENJEM M, VEMURI P, JONES D, KANTARCI K, WARD C, KOEPPE RA, FOSTER N, REIMAN EM, CHEN K, MATHIS C, LANDAU S, CAIRNS NJ, HOUSEHOLDER E, REINWALD LT, LEE V, KORECKA M, FIGURSKI M, CRAWFORD K, NEU S, FOROUD TM, POTKIN S, SHEN L, KELLEY F, KIM S, NHO K, KACHATURIAN Z, FRANK R, SNYDER PJ, MOLCHAN S, KAYE J, QUINN J, LIND B, CARTER R, DOLEN S, SCHNEIDER LS, PAWLUCZYK S, BECCERA M, TEODORO L, SPANN BM, BREWER J, VANDERSWAG H, FLEISHER A, HEIDEBRINK JL, LORD JL, MASON SS, ALBERS CS, KNOPMAN D, JOHNSON K, DOODY RS, MEYER JV, CHOWDHURY M, ROUNTREE S, DANG M, STERN Y, HONIG LS, BELL KL, ANCES B, MORRIS JC, CARROLL M, LEON S, MINTUN MA, SCHNEIDER S, et al. 2021. Four distinct trajectories of tau deposition identified in Alzheimer's disease. Nature Medicine, 27, 871–881.

WANG R, BENNER T, SORENSEN AG & WEDEEN VJ Diffusion toolkit: a software package for diffusion imaging data processing and tractography. Proc Intl Soc Mag Reson Med, 2007. Berlin.

WATERS J 2010. The concentration of soluble extracellular amyloid-β protein in acute brain slices from CRND8 mice. PloS one, 5, e15709–e15709. [PubMed: 21209950]

WILSON RJ 1979. Introduction to graph theory, Pearson Education India.

WOLK DA, DICKERSON BC & THE ALZHEIMER'S DISEASE NEUROIMAGING, I. 2010. Apolipoprotein E (APOE) genotype has dissociable effects on memory and attentional–executive network function in Alzheimer's disease. Proceedings of the National Academy of Sciences, 107, 10256.

WOOK YOO S, HAN CE, SHIN JS, WON SEO S, NA DL, KAISER M, JEONG Y & SEONG J-K 2015. A Network Flow-based Analysis of Cognitive Reserve in Normal Ageing and Alzheimer's Disease. Scientific Reports, 5, 10057. [PubMed: 25992968]

ZHOU J, GENNATAS, EFSTATHIOS D, KRAMER, JOEL H, MILLER, BRUCE L & SEELEY, WILLIAM W. 2012. Predicting Regional Neurodegeneration from the Healthy Brain Functional Connectome. Neuron, 73, 1216–1227. [PubMed: 22445348]

Highlights

1. Network flow-based model identifies tau propagation hubs in inferior temporal gyri
2. Remote Aβ-tau interactions in entorhinal cortex may trigger initial tau spreading
3. Local Aβ-tau interactions in inferior temporal gyrus may promote tau propagation
4. Connectivity-based model addresses the spatial incongruity between early Aβ and tau

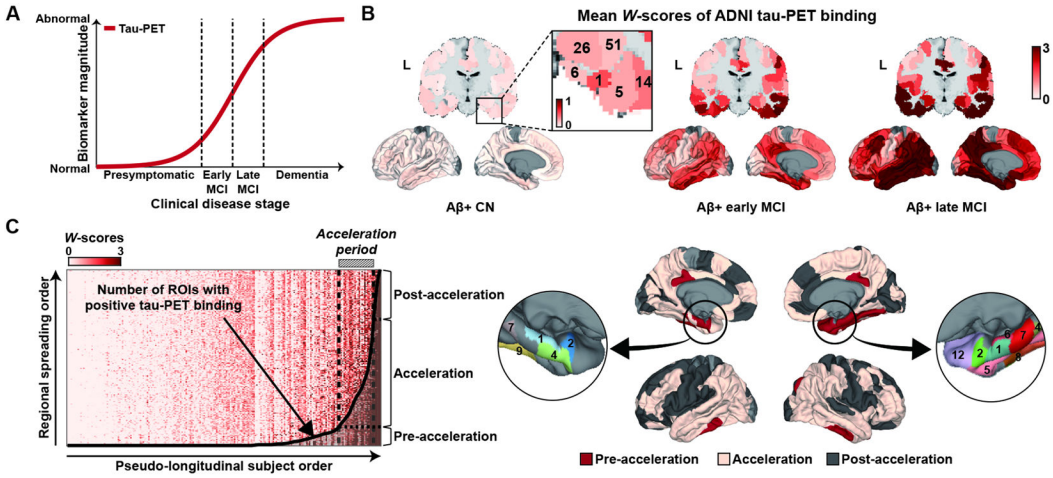

Figure 1. Pseudo-longitudinal tau regional spreading order.

A. Dynamic biomarker models of AD (Jack et al., 2010, Leuzy et al., 2019) propose that tau aggregation undergoes non-linear acceleration in early MCI. **B.** Tau-PET data from the ADNI cohort (present study) support this concept by demonstrating a sharp increase in brain-wide tau deposition that begins in Aβ+ subjects with early MCI and accelerates in late MCI. Color bar in Aβ+ CN inset indicates tau-PET *W*-scores. **C.** Across the presymptomatic and prodromal AD cohorts, we estimated the sequence of regional tau-PET positivity in a data-driven, pseudo-longitudinal manner, using the group-level frequency distribution to infer the order. Subjects were sorted based on the number of tau-PET-positive ROIs, and tau-PET-positive regions in subjects representing the pre-acceleration, acceleration, and post-acceleration periods are shown. The acceleration period was defined as beginning where the slope in the frequency graph becomes greater than two and ending where that slope shows a second inflection, such that the second derivative becomes zero. Number labels on magnified insets (panels **B** and **C**) show ranks, within each hemisphere, from the frequency distribution of tau-PET positivity. This approach identifies the entorhinal cortex (region labeled 1 in insets) as the most frequently tau-positive region, in keeping with cross-sectional neuropathological data (Braak and Braak, 1991). CN, cognitively normal; MCI, mild cognitive impairment.

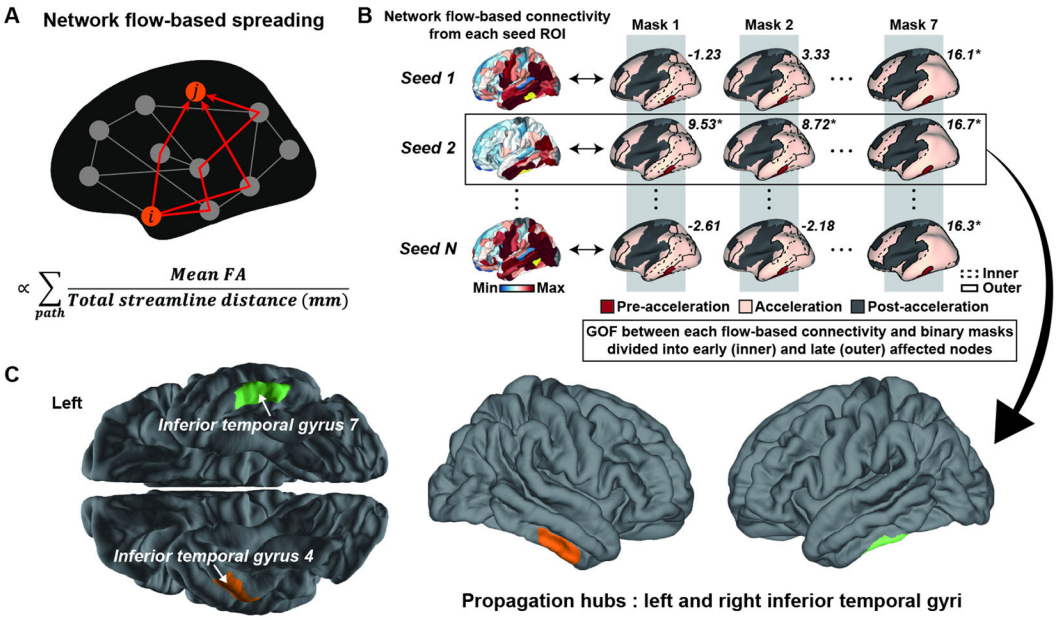

Figure 2. A network flow-based tau spreading model identifies tau propagation hubs in the inferior temporal gyri.

A. A simplified network graph illustrates the network flow-based propagation model of tau spreading. Circles represent brain regions (nodes), and lines represent structural connections between node pairs (edges). The network flow-based model adopts a definition of maximum inter-nodal flow, which considers multiple distinct paths. Tau spreading from node *i* to node *j* is proportional to the total flow value, which is calculated as the sum of the maximum flow for each possible path. **B.** Searching across all brain regions (examples in yellow shading), propagation hubs were identified based on the goodness-of-fit (GOF) of their network flow-based connectivity maps, derived from healthy controls, to 7 pairs of binary inner/outer masks defined using the regions that represent the tau acceleration phase (see Figure 1C and Methods; GOF scores from example seed ROIs are shown). **C.** Two regions were identified as propagation hubs, having significant GOF scores across all inner/outer mask thresholds, and both were subregions of the inferior temporal gyrus (ITG). FA, fractional anisotropy; ROI, region-of-interest.

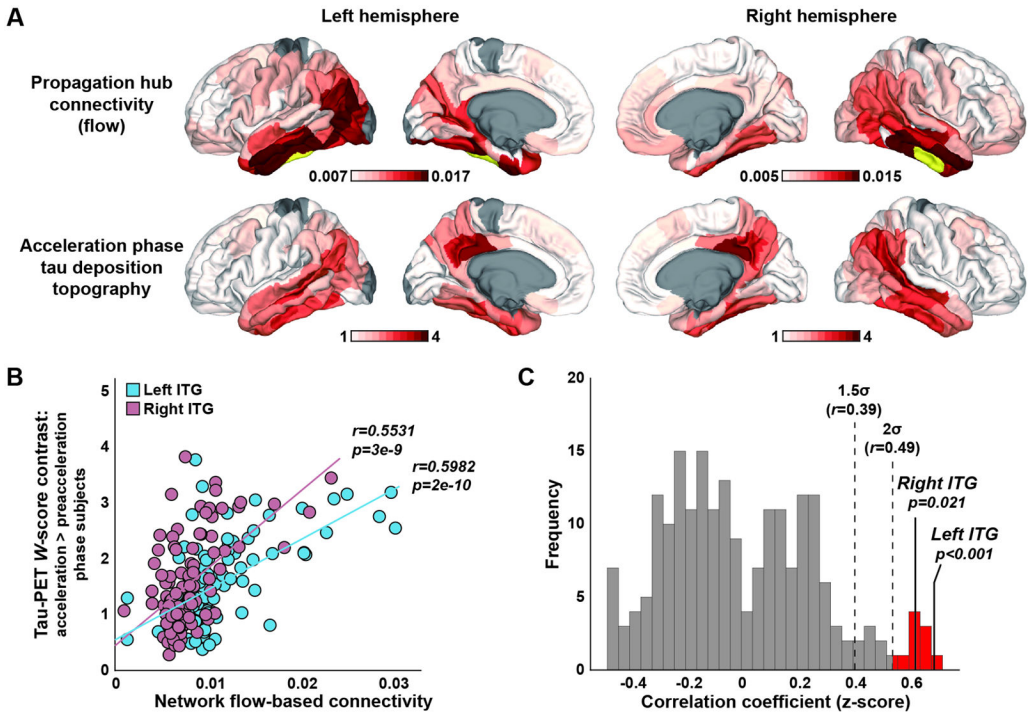

Figure 3. Inferior temporal gyrus connectivity mirrors tau acceleration phase topography.

A. Using the network flow-based model, we examined the connectivity patterns of the two inferior temporal gyrus regions (highlighted in yellow) identified as propagation hubs. The connectivity maps of these hubs resembled the acceleration phase tau deposition topography, derived by averaging *W*-score contrasts across all 1560 subject pairs representing the acceleration and pre-acceleration phases. **B.** The connectivity values and the acceleration phase tau deposition topography map show high spatial correlation for both hemispheres. **C.** Null hypothesis distributions are shown for spatial correlations between the total network flow-based maps and acceleration phase tau deposition topography. The correlation coefficients were converted to z-scores, and the corresponding one-tailed *p* values were obtained for the two ITG propagation hubs. The red areas show correlation coefficients more than 2 s.d. greater than the mean. ITG, inferior temporal gyrus.

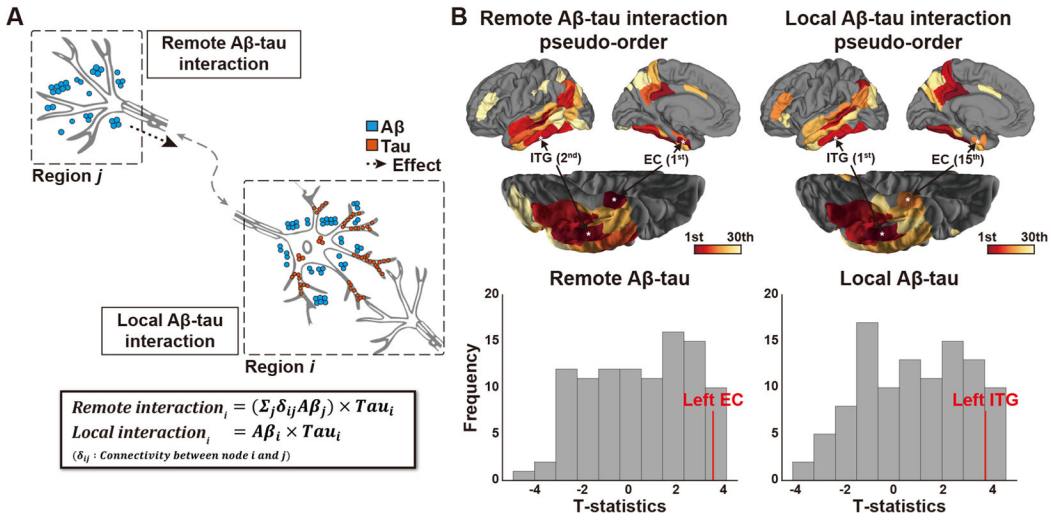

Figure 4. Network-based Aβ-tau interaction model.

A. Aβ-tau interactions were modeled using two interaction types: remote and local. Remote interaction measures the effect of Aβ deposition within regions to which a given region is connected, weighted by the strength of those connections, whereas local interaction requires the presence of Aβ and tau deposition within the same region. **B.** For remote Aβ-tau interactions, the lateral entorhinal cortex (EC) regions ranked first within the frequency distribution for each hemisphere. In contrast, the identified left and right ITG propagation hubs ranked first and second for local Aβ-tau interaction frequency within left and right hemisphere, respectively. T-statistic distributions of continuous remote Aβ-tau and local Aβ-tau interaction values also show greater interactions in the lateral EC and ITG, respectively, compared to other brain regions.

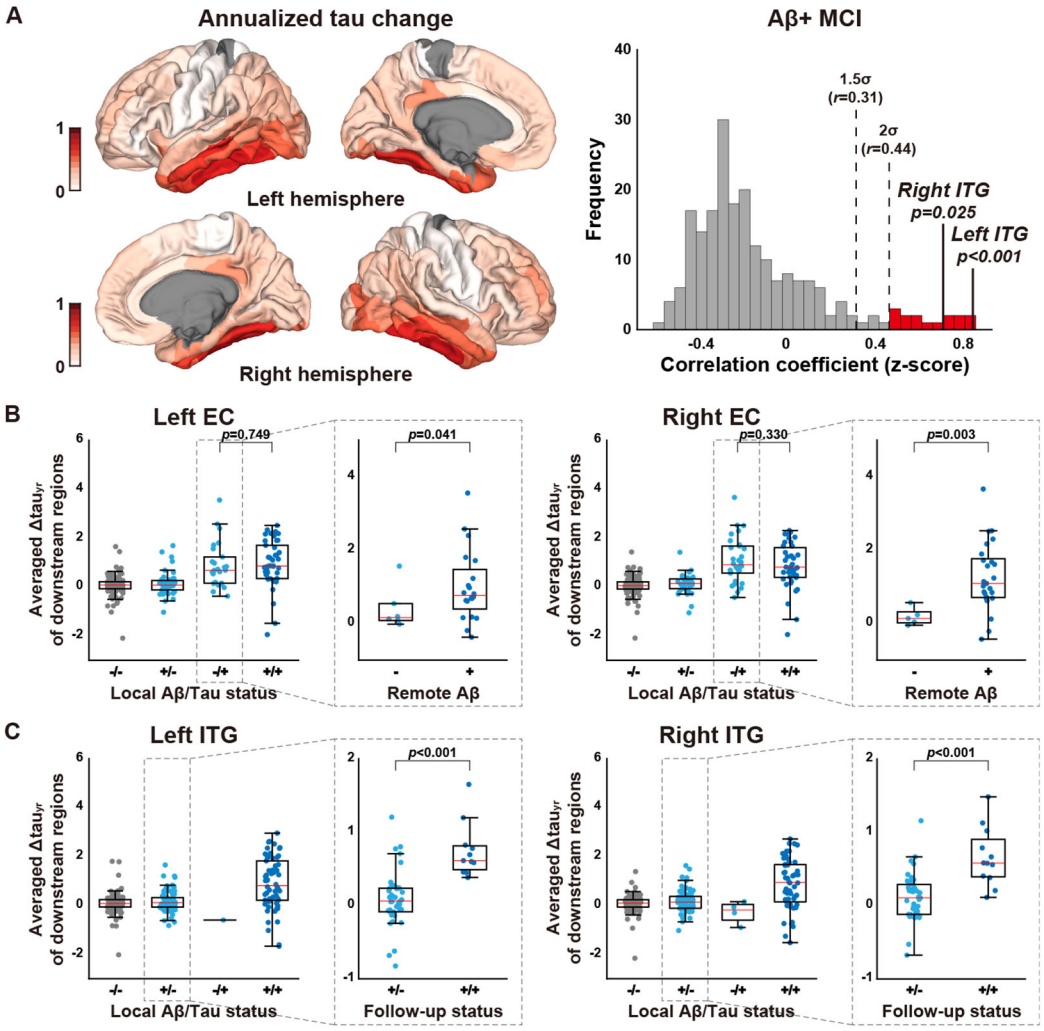

Figure 5. Longitudinal support for the network-based Aβ-tau interaction model.

A. In Aβ+ MCI subjects, tau-PET showed longitudinal tau accumulation in a regional pattern that strongly correlated with the network flow-based connectivity maps of the ITG propagation hubs. Correlation coefficients describing the relationship between each brain region's connectivity map and the Aβ+ MCI tau accumulation map were converted to z-scores and used to form a null hypothesis distribution; one-tailed *p* values were computed for the two ITG hubs. The red bars in the histogram show correlation coefficients more than 2 s.d. greater than the mean. **B-C**. The Aβ-tau interaction model was assessed longitudinally with the EC and ITG using the entire longitudinal dataset. For the EC (**B**), the subjects were classified into 4 subgroups according to the status of each region with respect to local Aβ and tau at baseline. In subjects with tau in the EC at baseline, local EC Aβ showed no effect on tau spreading. In subjects who lacked EC Aβ, however, those with remote, connectivity-based Aβ-tau interaction showed dramatically higher tau spreading than those without (**B** inset). In contrast, for the ITG regions (**C**), a transition to local Aβ-tau interaction was associated with significantly greater longitudinal tau accumulation in downstream regions (**C** inset).

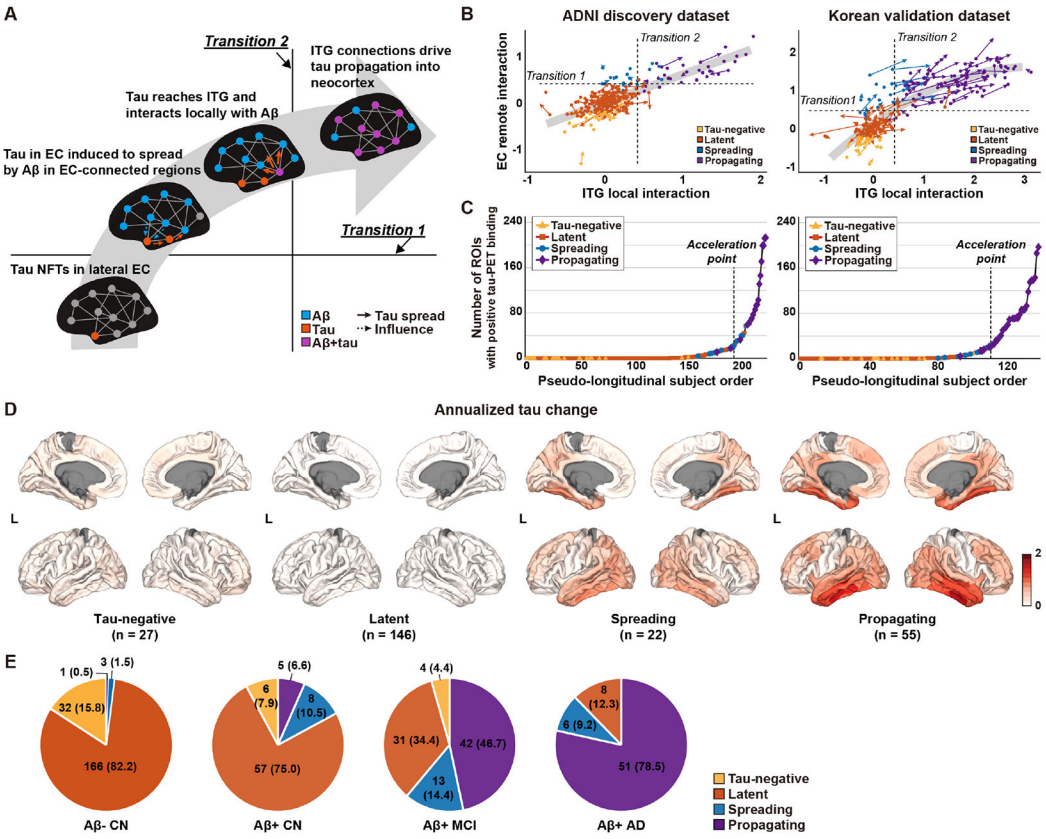

Figure 6. Two Aβ-tau interactions define a fundamental arc of AD molecular-anatomical progression.

A. Schematic representation of the AD progression model. **B.** Each subject's data are plotted, with an arrow connecting the baseline and follow-up scans (arrowhead points to later timepoint) where available. The nonlinear relationship between metrics representing EC remote Aβ-tau interaction and ITG local Aβ-tau interaction are supported by the overall trend in the data and support the notion that these phenomena represent a temporal progression. **C.** Subjects were stratified into four groups and overlaid on the pseudo-longitudinal subject order derived from the tau frequency distribution approach. Group color-coding in **B** and **C** indicates four tau group assignments at baseline. **D.** Annualized longitudinal tau *W*-score change maps, stratified by baseline tau group assignment, demonstrate the dramatic increase in tau spreading in the propagating tau group. **E.** Subjects from the ADNI and Korean Validation cohorts were stratified into four groups within each biomarker-anchored clinical label.

Table 1.

Demographic and clinical characteristics of the overall study population.

ADNI discovery dataset	**CN (n=182)**	**Early MCI (n=62)**	**Late MCI (n=30)**	**AD (n=9)**	**Group comparison p-value (statistics)**
Age (years)	75.29±7.77	75.79±6.82	74.77±7.56	69.56±10.0	0.309
Sex (female, *n* [%])	105 (57.7)	24 (38.7)	13 (43.3)	3 (33.3)	0.032 (8.835)
Education (years)	16.63±2.52	16.40±2.74	16.67±2.68	15.44±2.24	0.496
MMSE	28.96±1.32	27.43±3.13	25.63±5.56	21.44±1.67	<0.001
CDR SOB	0.16±0.52	1.98±2.47	2.97±3.56	3.83±1.62	<0.001
Amyloid positivity (%)*	67 (36.8)	28 (45.2)	17 (56.7)	9 (100.0)	<0.001 (17.194)
Korean validation dataset	**CN (n=96)**	**aMCI (n=84)**		**AD (n=71)**	**Group comparison p-value (statistics)**
Age (years)	66.31±9.49	71.32±9.12		74.37±9.35	<0.001
Sex (female, *n* [%])	60 (66.7)	51 (60.7)		54 (76.1)	0.093 (4.744)
Education (years)	11.94±4.54	11.46±4.26		9.77±5.72	0.047
MMSE	28.19±1.78	25.63±2.80		19.08±5.33	<0.001
CDR SOB	0.00±0.00	1.61±1.01		5.01±2.54	<0.001
Amyloid positivity (%)*	9 (9.4)	45 (53.6)		56 (78.9)	<0.001 (84.947)
Longitudinal dataset	**CN (n=146)**	**MCI (n=114)**		**AD (n=44)**	**Group comparison p-value (statistics)**
N (ADNI/Korean)	72/74	55/59		8/36	<0.001 (14.363)
Follow-up (years)	1.84±0.53	1.69±0.49		1.86±0.41	0.016
Age (years)	71.25±9.70	72.82±7.49		73.50±9.34	0.143
Sex (female, *n* [%])	88 (60.3)	59 (51.8)		30 (68.2)	0.135 (4.008)
Education (years)	14.22±4.16	13.73±4.46		10.27±5.74	<0.001
MMSE	28.59±1.60	26.46±3.27		20.52±4.15	<0.001
CDR SOB	0.12±0.46	1.38±1.31		4.39±1.64	<0.001
Amyloid positivity (%)*	40 (27.4)	68 (59.6)		36 (81.8)	<0.001 (51.199)

Data are presented as mean ± standard deviation for continuous variables and number (%) for nominal variables. Independent Kruskal-Wallis test for continuous variables and chi square test for nominal variables.

*Note that only amyloid-PET-positive subjects were included in subsequent analyses.

CN, cognitively normal; early MCI, early mild cognitive impairment; late MCI, late mild cognitive impairment; AD, Alzheimer's disease dementia; MMSE, mini-mental state examination; CDR SOB, clinical dementia rating sum-of-boxes; aMCI, amnestic mild cognitive impairment.

Key resources table

REAGENT or RESOURCE	SOURCE	IDENTIFIER
Deposited data		
Raw and analyzed data	ADNI	http://adni.loni.usc.edu/
Brainnetome atlas	(Fan et al., 2016)	http://www.brainnetome.org/
Software and algorithms		
MATLAB	Mathworks	https://www.mathworks.com/
FreeSurfer	Open source	http://surfer.nmr.mgh.harvard.edu/
FSL	FMRIB	https://fsl.fmrib.ox.ac.uk/fsl/
UCLA Multimodal Connectivity Package		https://github.com/jbrown81/umcp/
Custom MATLAB code		https://github.com/wjlee3/neuron_2022 DOI: 10.5281/zenodo.6387082